

# Dynamic Interfacial Reaction Rates from Electrochemistry-Mass Spectrometry

**Krempl, Kevin; Hochfilzer, Degenhart; Scott, Soren B.; Kibsgaard, Jakob; Vesborg, Peter C.K.; Hansen, Ole; Chorkendorff, Ib**

*Published in:*
Analytical Chemistry

*Link to article, DOI:*
10.1021/acs.analchem.1c00110

*Publication date:*
2021

*Document Version*
Peer reviewed version

# Dynamic Interfacial Reaction Rates from Electrochemistry - Mass Spectrometry

Kevin Krempl,[†] Degenhart Hochfilzer,[†] Soren B. Scott,[‡] Jakob Kibsgaard,[†] Peter C. K. Vesborg,[†] Ole Hansen,[¶] and Ib Chorkendorff[*,†]

† *Department of Physics, Technical University of Denmark, DK-2800 Kgs. Lyngby, Denmark*

‡ *Department of Materials, Imperial College London, SW7 2AZ, UK*

¶ *DTU Nanolab, Technical University of Denmark, DK-2800 Kgs. Lyngby, Denmark*

E-mail: ibchork@fysik.dtu.dk

## Abstract

Electrochemistry - mass spectrometry is a versatile and reliable tool to study interfacial reaction rates of faradaic processes with high temporal resolution. However, measured mass spectrometric signals typically do not directly correspond to the partial current density towards the analyte due to mass transport effects. Here we introduce a mathematical framework, grounded on a mass transport model, to obtain a quantitative and truly dynamic partial current density from a measured mass spectrometer signal by means of deconvolution. Further, it is shown that the time resolution of electrochemistry - mass spectrometry is limited by entropy driven processes during mass transport to the mass spectrometer. The methodology is validated by comparing measured impulse responses of the hydrogen and oxygen evolution to the model predictions and subsequently applied to uncover dynamic phenomena during hydrogen and oxygen evolution in acidic electrolyte.

## Introduction

Electrochemistry - mass spectrometry (EC-MS) was pioneered by Bruckenstein and Gadde[1] and has since its further development in the 1980s[2] matured into a highly versatile and reliable tool to study electrochemical reactions, ranging from $CO/CO_2$ reduction,[3,4] water splitting,[5–7] hydrocarbon oxidation[8,9] and metal dissolution[10] to non-aqueous chemistries such as electrolyte and cathode decomposition reactions relevant for Li-ion batteries.[11–14] Recent iterations of EC-MS are able to reach impressive temporal resolution,[15–17] which makes it possible to study the dynamic behaviour of electrochemical reactions. This ability is particularly important for studying deactivation mechanisms or the effect of load variations, both relevant for practical applications, as well as for more fundamental aspects such as mechanism discrimination or transient activity measurements. Moreover, in contrast to ex-situ quantification methods such as chromatography or colorimetric reactions, a high temporal resolution EC-MS experiment enables rapid activity assessment of a given catalyst. This has the potential to significantly speed-up the development of new catalysts and interfaces for electrochemical energy conversion devices urgently needed for a transition towards a more sustainable energy system.[18] The fundamental quantity of interest in EC-MS is the interfacial reaction rate or partial current density towards a given product, whether gaseous, liquid or in ionic form. This partial current cannot be obtained by a simple electrochemical mea-

surement as unknown side reactions as well as capacitive and pseudo-capacitive processes also contribute to the total measured current. It has been shown that even for apparently simple reactions such as hydrogen and oxygen evolution, the measured current doesn't necessarily correspond to the partial current towards the given product and it is therefore necessary to independently quantify reaction products. In this regard, mass spectrometry sets itself apart from other quantitative analytical techniques used in electrochemical research, in that it can measure a continuous flux of ions hitting the detector. However, only under (quasi)-steady-state conditions is the partial current density proportional to the flux measured by the mass spectrometer. Decreasing the time until a steady-state is reached, often termed the time-response, while maintaining a high collection efficiency of the analyte, has therefore become a paramount design criterion for EC-MS experiments.[15,19,20] While a further reduction of the time response of EC-MS experiments is limited by practical considerations, such as mass transport of reactants to the electrode or the uncompensated resistance of the electrochemical cell, the goal of this paper is to layout and verify a general mathematical procedure to back-calculate the partial current density from a measured mass spectrometer signal under dynamic conditions. The ability to obtain truly dynamic EC-MS measurements is then demonstrated for hydrogen and oxygen evolution on platinum electrodes in acidic electrolyte and the effect of transient oxide growth on oxygen evolution activity is for the first time investigated under dynamic operating conditions.

# Experimental

All data treatment is carried out using the open-source *Python* libaries *numpy*,[21] *scipy* and *mpmath* and the developed methodology is implemented in the open-source *ixdat* python package. The underlying differential equations are derived and solved analytically as described in detail in the Supporting Information. The inverse Laplace transform is calculated numerically using the Talbot method as implemented in the *mpmath* package and deconvolution is carried out by Wiener deconvolution whereby the discrete fourier transforms are calculated by the Fast Fourier Transform algorithm as implemented in *numpy*. The *Python* scripts and the raw-data to reproduce the presented plots are made available here *github.com/kkrempl/Dynamic-Interfacial-Reaction-Rates*.

The experiments were carried out with a commercially available microchip-based EC-MS instrument (SpectroInlets ApS, Denmark) with a stagnant electrolyte cell, which is described in detail by Trimarco et al.[16] Unless otherwise stated, helium (6.0, Air Liquide) was used as an auxiliary gas. For the electrochemical experiments 0.1 M $HClO_4$ was prepared from $HClO_4$ (70 %, Suprapur, Merck KG) and ultra pure water (Millipore). The platinum disk working electrode (99.95 %, MaTek) was polished with diamond paste (0.25 µm, Struers GmbH) on a micro-polishing cloth and subsequently rinsed and sonicated once in ethanol and once in ultra pure water before being flame annealed. A leak-less Ag/AgCl reference electrode (Innovative Instruments Inc.) together with a Pt-wire (99.99 %, Goodfellow) counter electrode separated by a ceramic frit was used. The reference electrode was calibrated against a reversible hydrogen electrode in a separate electrochemical cell by measuring the open-circuit voltage of a Pt wire in hydrogen saturated 0.1 M $HClO_4$ electrolyte after a reductive pretreatment. If not stated otherwise, all stated potentials refer to the potential versus the reversible hydrogen electrode. Before initiating the galvanic and potential step experiments as well as the impulse response measurements, the Pt electrode was cycled between 0.0 $V_{RHE}$ and 1.5 $V_{RHE}$ until a steady-state voltammogram (Figure S1) was obtained. Calibration was carried out before each measurement. Therefore, the hydrogen signal in the mass spectrometer was calibrated by galvanostatic measurements at $-0.05\,mA\,cm^{-2}$, $-0.10\,mA\,cm^{-2}$ and $-0.15\,mA\,cm^{-2}$. Before the oxygen calibration, a galvanostatic anodization treatment at $0.15\,mA\,cm^{-2}$ was carried out for at least

ten minutes until a steady state oxygen signal was reached. This ensures a 100% faradaic efficiency and avoids any charge lost to surface oxidation. Thereafter, the calibration was carried out galvanostatically at $0.15\,\mathrm{mA\,cm^{-2}}$, $0.10\,\mathrm{mA\,cm^{-2}}$ and $0.05\,\mathrm{mA\,cm^{-2}}$. Impulse response measurements were carried out by applying a reductive impulse at -0.5 $\mathrm{V_{RHE}}$ between 10 ms and 100 ms during a galvanostatic hold at $-0.10\,\mathrm{mA\,cm^{-2}}$ for hydrogen and by applying a oxidative impulse at 2 $\mathrm{V_{RHE}}$ between 20 ms and 200 ms during a potentiostatic hold at 1.4 $\mathrm{V_{RHE}}$.

The ionization energy of the mass spectrometer (PrismaPro, Pfeiffer GmbH) was set to 70 eV and the voltage at the secondary electron multiplier (SEM) detector was set to 1200 V. For hydrogen detection the dwell time at m/z=2 was set to 68 ms with a 32 ms lead-in time, resulting in a 10 Hz sampling frequency. On the other hand, oxygen at m/z=32 was measured with a dwell-time of 128 ms and 32 ms lead-in time to achieve a reasonable signal-to-noise ratio at a sampling frequency of 6.6 Hz.

# Results and Discussion

## Mathematical framework

The mathematical relation between the partial current density and the measured mass spectrometer signal in general depends on the non-steady-state mass transport of the analyte between the electrode-electrolyte interface and the detector of the mass spectrometer. This includes convective-diffusive mass transport under the ambient conditions inside the electrochemical cell together with molecular flow under UHV conditions. While the detailed derivation, non-dimensionalization and analytical solution of the governing differential equations can be found in the Supporting Information, the following section outlines the general mathematical framework of how to obtain a partial current density from a calibrated mass spectrometer signal.

The mass transport in the stagnant thin-layer electrochemical cell is described by Fick's law of diffusion and was presented earlier by Trimarco et al.[16] Thereby, the assumption is made that the analyte does not interact chemically with the electrolyte. An exeption to this is for example $CO_2$, which is in equilibrium with $H_2O$ to form carbonic acid.[22] As boundary conditions a time dependant flux at the electrode $\dot{n}_i(t)$ is chosen to represent the partial current density $J_i(t)$ towards a given analyte, and Henry's law, with the dimensionless Henry volatility $k_H$, is applied at the gas-liquid interface between the electrolyte and the nano-sized gas sampling volume inside the microchip at $x = 0$. Instead of using the full convection-diffusion equation to describe the mass transport in the gas sampling volume, the transport can be simplified by assuming a ideally mixed gas due to the fast gas phase diffusion of the analyte. After non-dimensionalization, the following system of coupled differential equations is obtained

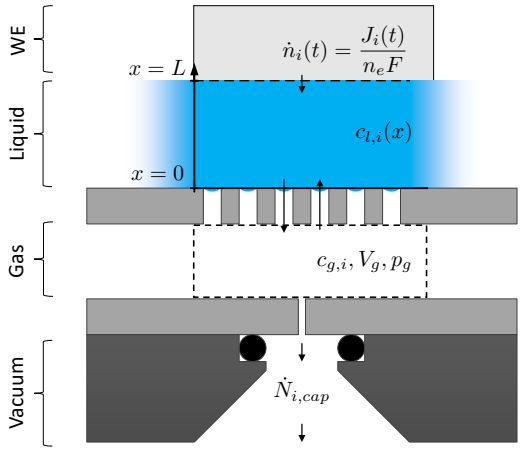


Figure 1: Schematic diagram (not to scale) of the mass transport of the analyte $i$ produced with a molar flux $\dot{n}_i(t)$ or partial current density $J_i(t)$ at the electrode surface at $x = L$. For detailed derivation and non-dimensionalization of the governing differential equations see Supporting Information.

$$\frac{\partial \hat{c}_{l,i}}{\partial \hat{t}} = \frac{\partial^2 \hat{c}_{l,i}}{\partial \hat{x}^2} \tag{1}$$

$$\left.\frac{\partial \hat{c}_{l,i}}{\partial \hat{x}}\right|_{\hat{x}=1} = \hat{n}_i(\hat{t}) \tag{2}$$

$$\hat{c}_{l,i}(\hat{x}=0) = \frac{1}{k_H}\hat{c}_{g,i} \tag{3}$$

$$\frac{d\hat{c}_{g,i}}{d\hat{t}} = \kappa \frac{\partial \hat{c}_{l,i}}{\partial \hat{x}}\Big|_{\hat{x}=0} - \hat{c}_{g,i}\lambda. \quad (4)$$

Here, $\hat{c}_{g,i}$ and $\hat{c}_{l,i}$ are the dimensionless concentration of the analyte $i$ in the gas and liquid respectively, $\hat{x}$ corresponds to the dimensionless distance from the electrode, whereby $\hat{x} = 0$ is the liquid-gas interface, and $\hat{t}$ is the dimensionless diffusional time-scale in the liquid. To calculate the inverse of the dimensionless gas phase residence time $\lambda$, the capillary volume flow $\dot{V}_{cap}$ is divided by the gas sampling volume $V_g$ and by the characteristic diffusion time. The capillary volume flow $\dot{V}_{cap}$ was in turn calculated by an analytical expression, which was presented and confirmed in earlier publications.[23–25] Finally, the mass transport in the UHV environment may also have significant influence on the time-response of the EC-MS experiment because of the limited pumping speed through the tubing leading to the ionization unit. With this in mind, the amount of tubing between the capillary and the ionization unit was kept at a minimum and a wide inner diameter was chosen to ensure high pumping speeds. By varying the tubing length, it was shown that the mass transport in UHV has a negligible influence on the time-response of the system (Figure S2) as long as the tubing is kept to a minimum. By then solving the differential equations in Eq. 1 to 4 analytically using the Laplace transform, it can be shown that the mass spectrometer signal equals the convolution integral of the dimensionless flux at the electrode with the impulse response of the system $h(\hat{t})$ (Eq. 5). Consequently, the flux at the electrode, which can be converted into a partial current density according to Faraday's law of electrolysis, can be obtained by deconvoluting the impulse response $h(\hat{t})$ from a calibrated mass spectrometer signal.

$$\hat{c}_g(\hat{t}) = \int_0^\infty \hat{n}(\tau) h(\hat{t} - \tau)\, d\tau, \quad (5)$$

where $h(\hat{t}) = \mathcal{L}^{-1}\{H(\hat{s})\}(\hat{t})$ and

$$H(\hat{s}) = \frac{1}{k_H \frac{\hat{s}+\lambda}{\kappa} \cosh(\sqrt{\hat{s}}) + \sqrt{\hat{s}} \sinh(\sqrt{\hat{s}})}. \quad (6)$$

Here $\mathcal{L}^{-1}$ represents the inverse Laplace transform, which can be calculated numerically (see SI). For discrete values of $\hat{t}$ as it is the case in practical measurements, Eq. 5 can be rewritten in matrix notation as

$$\mathbf{c} = \mathbf{H} \cdot \mathbf{n} \quad (7)$$

with $\mathbf{n} = (n_0, n_1, ...n_{n-1})^T, \mathbf{c} = (c_0, c_1, ...c_{n-1})^T$ and

$$\mathbf{H} = \begin{pmatrix} h_0 & h_1 & h_2 & \cdots & h_m \\ h_m & h_0 & h_1 & \cdots & h_{m-1} \\ h_{m-1} & h_m & h_0 & \cdots & h_{m-2} \\ \vdots & \vdots & \vdots & \ddots & \vdots \\ h_1 & h_2 & h_3 & \cdots & h_0 \end{pmatrix}, \quad (8)$$

where $h_{i-j} = h(t_i - t_j)$. Here $t_j = t_0 + j\Delta t$, $n_j = \hat{n}(t_j)$ and $c_j = \hat{c}_g(t_j)$.

As long as the convolution matrix $\mathbf{H}$ is invertible there is a unique solution to this problem. However, due to the ill-conditioned nature of deconvolution problems, small deviations in the measured data of $\hat{c}_g(\hat{t})$, such as noise, can lead to large changes in the computed output.

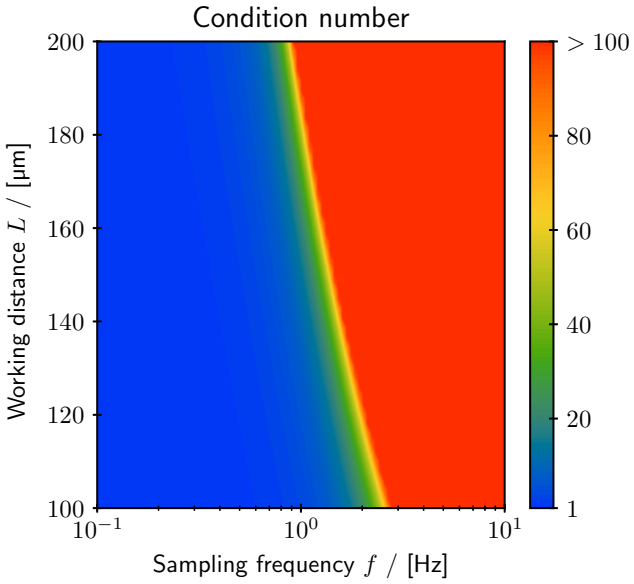


Figure 2: Condition number of the convolution matrix $\mathbf{H}$ as a function of working distance $L$ and sampling frequency $f$. The analyte is assumed to be hydrogen ($k_H$=52, $D$=5.05 × $10^{-9}$ m$^2$ s$^{-1}$) with $\dot{V}_{cap}$=137 nl s$^{-1}$ and $V_g$=100 nl. High values of the condition number imply a low signal-to-noise ratio of the deconvoluted partial current density.

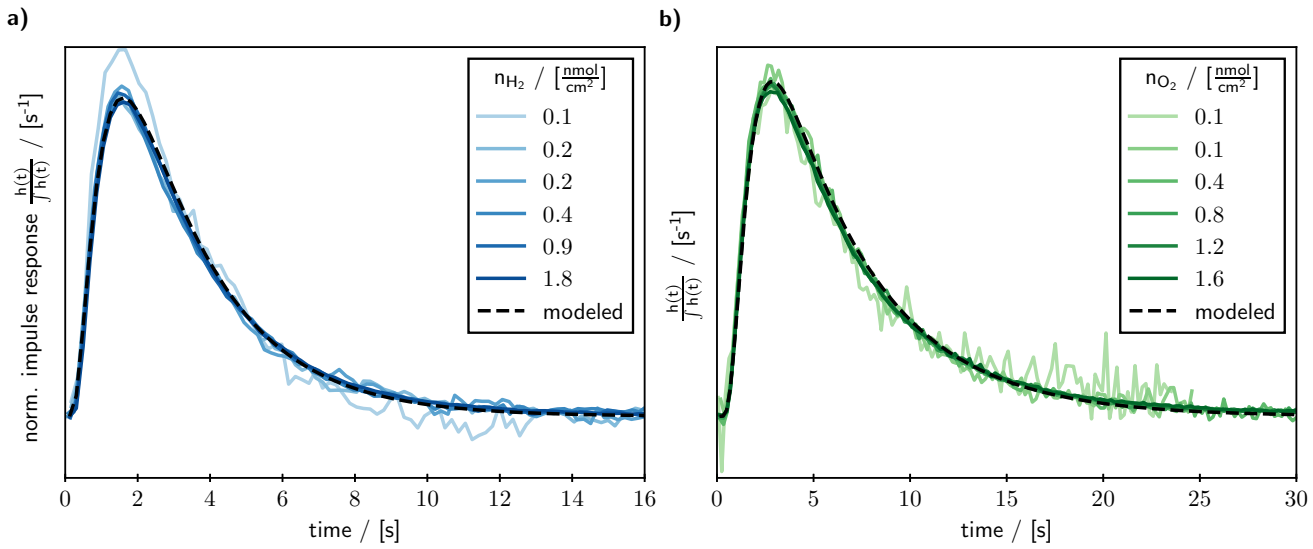


Figure 3: Comparison between modeled ($L$=150 µm, $\dot{V}_{cap}$=137 nl s$^{-1}$, $V_g$=100 nl) and measured impulse response for (a) hydrogen ($k_H$=52, $D$=5.05 × 10$^{-9}$ m$^2$ s$^{-1}$) and (b) oxygen ($k_H$=33, $D$=2.1 × 10$^{-9}$ m$^2$ s$^{-1}$). Varying amounts of evolved analyte were obtained by varying the time of the impulse up to 200 ms, which is well below $\frac{1}{f_{\text{lim}}}$.

Figure 2 shows the condition number, defined as

$$\text{cond}(\mathbf{H}) = \|\mathbf{H}\| \cdot \left\|\mathbf{H}^{-1}\right\|, \tag{9}$$

as a function of working distance $L$ and sampling frequency $f$. A higher condition number implies that small changes in the input lead to larger changes in computed output or, in other words, implies a lower signal-to-noise ratio of the computed output.[26] Further, as the condition number approaches infinity the matrix becomes degenerated and a unique solution cannot be obtained anymore. In a more physical sense the non-uniqueness of the solution to this inverse mass transport problem arises from the second law of thermodynamics. Since the diffusion through the electrolyte volume and the diffusional mixing inside the gas sampling volume are entropy driven, information about the partial current density must be lost in the process. This is reflected by a rapidly increasing condition number when approaching a certain sampling frequency $f_{\text{lim}}$ as displayed in Figure 2. Frequency components of the partial current density above $f_{\text{lim}}$ are therefore irreversibly lost due to the second law of thermodynamics and cannot be reconstructed by deconvolution. The mass transport between the electrode-electrolyte interface and the mass spectrometer can therefore be thought of as a thermodynamic low-pass filter that attenuates high frequency components of the partial current density. For typical values of the mass transport parameters in the system under study, $f_{\text{lim}}$ lies above 1 Hz, which has important implications when drawing conclusions on the absence or presence of transient reaction events at the electrode-electrolyte interface. Even a mass spectrometer with an infinitely fast sampling rate and infinitely high sensitivity would not be able to detect transient behaviour with frequency components above $f_{\text{lim}}$ as the transient would be blurred by diffusion. This shows, that the mass transport between the electrode-electrolyte interface and the UHV of the mass spectrometer is, besides the sensitivity of the mass spectrometer, an important factor to consider when designing EC-MS experiments studying the dynamics of electrochemical reactions. Further, the presented procedure of deconvolution as well as condition number analysis can generally be applied to any kind of EC-MS experiment even without a analytical mass transport model at hand since the impulse response $h(\hat{t})$ required to construct the

convolution matrix can also be measured experimentally as described in the following section.

## Experimental validation

Having demonstrated the mathematical feasibility of obtaining the partial current density from a measured mass spectrometer signal by deconvolution, the underlying mass transport model is validated experimentally. So far, the impulse response $h(\hat{t})$ was only treated theoretically. However, $h(\hat{t})$ can also be directly measured by applying a very short ($t < \frac{1}{f_{lim}}$) impulse of analyte production at the electrode and measuring the corresponding mass spectrometer signal. Such impulse response methods are also commonly used in heterogeneous catalysis research in order to measure the mass transport properties or residence time distributions of chemical reactors.[27] Mathematically, a very short impulse of analyte production at the interface corresponds to $\hat{n_i}(\hat{t})$ being a delta function at $\hat{t} = 0$. Because the integral of this delta function in Eq. 5 is unity, the measured mass spectrometer signal directly equates to $h(\hat{t})$. To validate the model, the impulse responses for hydrogen and oxygen evolution are measured and then compared to the mass transport model. The diffusion constant $D_i$ and the dimensionless Henry volatility $k_H$ for hydrogen and oxygen are thereby obtained from literature,[28–30] whereas the exact working distance $L$ is determined by fitting to the measured impulse response. The accuracy of the obtained value for the working distance $L$ was further confirmed by measuring the mass transport limited hydrogen oxidation current, which agrees well with the value obtained from the impulse response (see Supporting Information). The gas sampling volume $V_g$ is per design 100 nl and the capillary flow $\dot{V}_{cap}$ ($\sim$100 nl s$^{-1}$) is determined as described in a previous publication.[8] Figure 3 shows the measured area-normalized impulse responses for different amounts of evolved analyte in comparison to the model predictions. The measured area-normalized impulse responses match well with the model predictions independent of the amount of evolved analyte, which is important to ensure accurate deconvolution. The predicted impulse response also matches well with the measured one for hydrogen and oxygen respectively, meaning that the difference in molecular properties ($k_H$, $D_i$) between hydrogen and oxygen is accurately captured by the model. To further substantiate the accuracy of the model, measurements for varying working distances $L$ and capillary flows $\dot{V}_{cap}$ are also carried out and agree well with the model predictions (Figure S3 and S4).

## Dynamic partial current densities of hydrogen and oxygen evolution at platinum electrodes

First, a series of hydrogen evolving galvanic steps are carried out as displayed in Figure 4a. Here, deconvolution of the measured mass spectrometer signal with the impulse response yields an almost quantitative match between measured faradaic current (Figure 4a lower pannel) and deconvoluted partial current density (Figure 4a upper pannel). Only during the first galvanic step, a slight transient towards a steady state is observed within the first 2 s (Figure 4a inset upper panel) indicating that not all of the passed charge goes towards evolving hydrogen. This unaccounted charge can most likely be ascribed to hydrogen underpotential deposition (H-UPD). As the experiments are not carried out under hydrogen saturation, hydrogen is evolved already at potentials positive of RHE leading to a overlap with H-UPD[31] region.

A representative potential step from 0.35 $V_{RHE}$ to a hydrogen evolving potential of 0.01 $V_{RHE}$ is depicted in Figure 4b showing a high initial deconvoluted partial current density, which decays towards a steady state value (Figure 4b upper panel). This dynamic behaviour is also reflected in the measured current transient (Figure 4b lower panel). The reason for this dynamic behaviour of HER upon a potential step can be explained by the reversible nature of the HER/HOR couple on platinum electrodes in acidic electrolyte leading to Nernstian behaviour.[32] In the beginning of the potential step no hydrogen is present at the

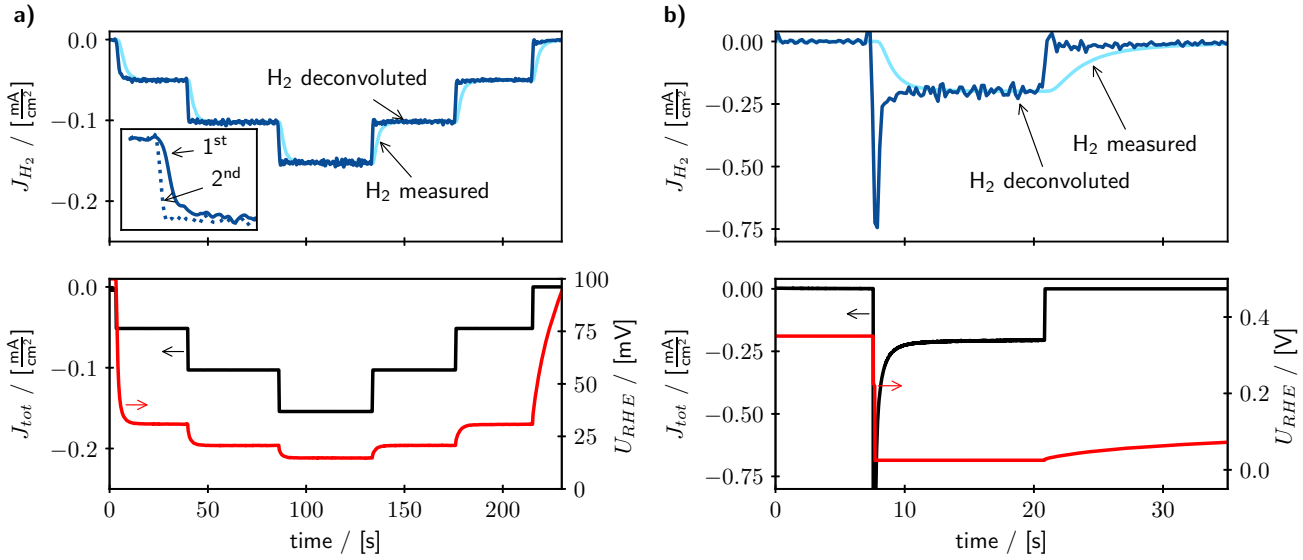


Figure 4: Deconvoluted partial current density in comparison to the measured MS signal of hydrogen evolution for (a) a series of galvanic steps and (b) a potential step. Upper panels show the measured MS signal at 2 amu together with the deconvoluted partial current density, whereas the lower panels show the measured total current density and voltage from the potentiostat. The inset in (a) shows the deconvoluted partial current density for hydrogen of the first (solid) and second (dotted) galvanic step, highlighting the transient behaviour in the first step.

interface and therefore the back-reaction, HOR, does not occur leading to a high initial HER rate. However, as soon as hydrogen is generated at the interface, the back-reaction occurs as well, decreasing the net-rate of hydrogen evolution until a steady state is reached.[33] While hydrogen evolution is the only faradaic reaction occurring in the previous examples, the quantitative aspect of the presented methodology becomes particular important when multiple competing reactions occur at the electrode. In the case of oxygen evolution at Pt electrodes, dynamic behaviour arises from the interplay between oxygen evolution and the formation of an insulating $PtO_2$ species according to Eq. 10.

$$Pt + 2\,H_2O \longrightarrow PtO_2 + 4\,H^+ + 4\,e^- \qquad (10)$$

This is reflected by a transient decrease of the total current density $J_{tot}$ obtained upon a potential step from a potential of $0.55\,V_{RHE}$ to an oxygen evolving potential of $1.60\,V_{RHE}$ (see Figure 5a lower panel). Moreover, the evolved oxygen cannot account for all of the measured total current density particularly in the first 20 seconds after the potential step. Therefore, this unaccounted current most likely goes towards formation of the $PtO_2$ layer and the partial current density towards $PtO_2$ $J_{PtO_2}$ can be calculated as the difference between the measured total current density $J_{tot}$ and the deconvoluted partial current density of oxygen $J_{O_2}$. Both, the oxygen evolution as well as the $PtO_2$ formation rate, decrease over time. This is due to $PtO_2$ beeing an insulator and therefore acting as a tunnel barrier for the electron transfer slowing down the faradaic reactions. Thereby, the faradaic reaction rate decreases exponentially with the thickness of the tunnel barrier as shown theoretically and experimentally by Schultze et al.[34,35] For the potential step in Figure 5a, the $PtO_2$ thickness $d_{PtO_2}$ can be calculated by assuming a 4-electron process and $PtO_2$ having a density of $\rho_{PtO_2}$=11.25 g cm$^{-2}$ as followed,[36]

$$d_{PtO_2}(t) = \int_0^t \frac{J_{PtO_2}(\tau) M_{PtO_2}}{4F\rho_{PtO_2}} d\tau. \qquad (11)$$

By plotting the $PtO_2$ thickness against the logarithm of the partial current density towards oxygen $J_{O_2}$ as in Figure 5b, the same relation-

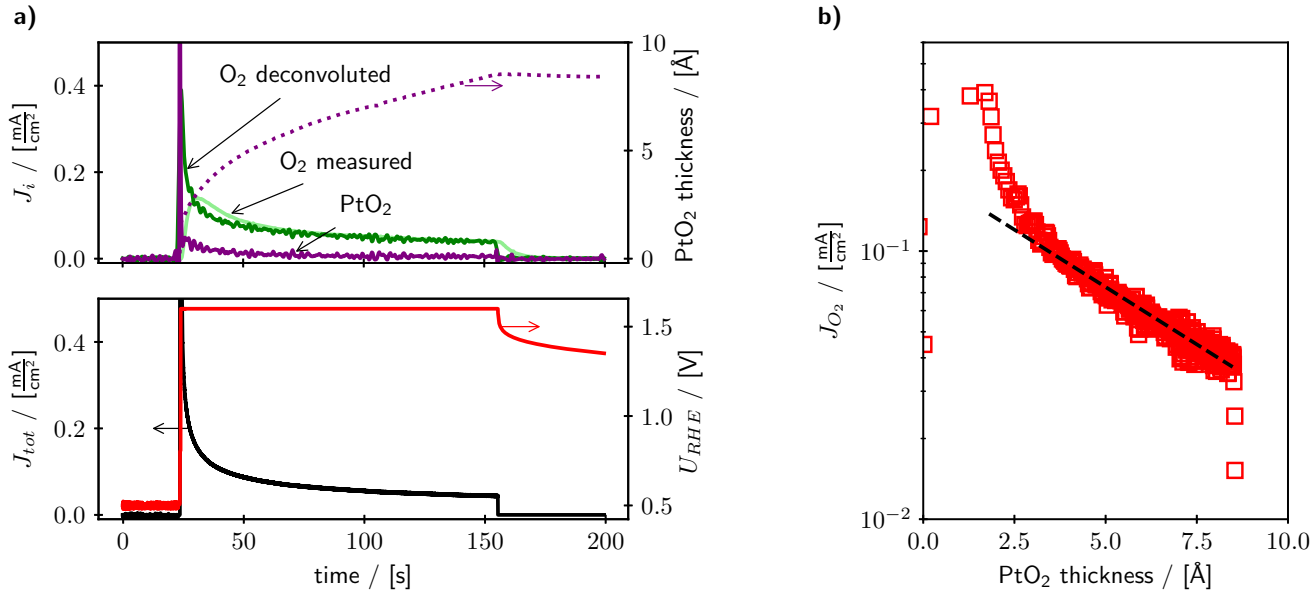


Figure 5: (a) The upper panel shows the deconvoluted partial current density of OER (including the measured MS signal) and $PtO_2$ formation together with the calculated thickness of the formed oxide during a potential step experiment. Lower panel shows the total current density and voltage as measured by the potentiostat. (b) OER partial current density plotted against the calculted oxide thickness during the potential step experiment displayed in a.

ship was found for the measurements carried out in this study. Further, by extrapolating the exponential region to zero thickness, the intrinsic OER activity of the $PtO_2$ surface can be estimated. The exponential behaviour is however only observed for thicknesses above 3.5 Å, which roughly corresponds to the thickness of one monolayer of $PtO_2$.[36] Before this thickness, a higher activity is observed, which even exceeds the extrapolated value at zero thickness. On the other hand, this behavior is not observed for a potential step from 1.3 $V_{RHE}$ to 1.6 $V_{RHE}$, where the Pt surface has been anodized prior in order to build up an oxide layer (Figure S5). Consequently, the partially oxygen-covered metallic platinum surface, that only exists transiently within the first seconds after the potential step, appears to be more active towards OER than the $PtO_2$ surface. This is in line with earlier theoretical studies by Rossmeisl et al., who have found a partially oxygen-covered metallic Pt surface to have a high OER activity, beeing close to the top of the activity volcano.[37] This shows that a fully dynamic, high time resolution EC-MS experiment in combination with the herein developed methodology allows insight into previously inaccessible dynamic phenomena occurring at the electrode-electrolyte interface.

# Conclusion and Outlook

A general procedure, based on deconvolution of mass transport effects from a calibrated mass spectrometer signal, was introduced to obtain dynamic partial current densities from EC-MS experiments. For the first time, dynamic phenomena occurring during hydrogen and oxygen evolution, which have been extensively studied with electrochemical methods, are quantitatively resolved from EC-MS measurements. This extends the capabilities of EC-MS experiments to a wide array of dynamic electrochemical methods such as potential and galvanic step experiments as well as high scan-rate cyclic voltammetry and has the potential to speed up the development of novel catalysts and interfaces for important energy conversion reactions. The methodology is thereby applicable to any interfacial reaction, even for

such where the educts are depleted from the interface. For example, the dynamic interplay between oxygen evolution and oxide growth, which was investigated on platinum electrodes here, may foster new insight and design criteria for novel oxygen evolving electrocatalysts. Moreover, the transient behaviour of the complex $CO_2$ reduction reaction during potential step experiments can yield new insights into the rate-determining step or the relevance of certain intermediate species towards high-value products such as ethylene and ethanol.[38] It has also been shown that dynamic electrolysis yields improved faradaic efficiencies for many different electrochemical reactions.[39–41] Exact knowledge of the interfacial reaction rate during the pulses may significantly simplify the optimization of such strategies towards improved efficiencies.

# Supporting Information

Figure S1: Steady-state cyclic voltammogram of the Pt electrode; Equation 1-26: Derivation of the mass transport model and deconvolution procedure; Figure S2: Influence of vacuum mass transport on impulse response; Figure S3: Influence of working distance on impulse response; Figure S4: Influence of capillary flow on impulse response; Figure S5: Potential step experiment of a oxidized Pt surface.

# Acknowledgements

Supported by the Villum Foundation V-SUSTAIN grant 9455 to the Villum Center for the Science of Sustainable Fuels and Chemicals.

# References


(1) Bruckenstein, S.; Gadde, R. R. Use of a porous electrode for in situ mass spectrometric determination of volatile electrode reaction products. *J. Am. Chem. Soc.* **1971**, *93*, 793–794.

(2) Wolter, O.; Heitbaum, J. Differential Electrochemical Mass Spectroscopy (DEMS) - a New Method for the Study of Electrode Processes. *Ber. Bunsenges. Phys. Chem.* **1984**, *88*, 2–6.

(3) Clark, E. L.; Bell, A. T. Direct Observation of the Local Reaction Environment during the Electrochemical Reduction of CO 2. *J. Am. Chem. Soc.* **2018**, *140*, 7012–7020.

(4) Löffler, M.; Khanipour, P.; Kulyk, N.; Mayrhofer, K. J.; Katsounaros, I. Insights into Liquid Product Formation during Carbon Dioxide Reduction on Copper and Oxide-Derived Copper from Quantitative Real-Time Measurements. *ACS catal.* **2020**, *10*, 6735–6740.

(5) Roy, C.; Sebok, B.; Scott, S. B.; Fiordaliso, E. M.; Sørensen, J. E.; Bodin, A.; Trimarco, D. B.; Damsgaard, C. D.; Vesborg, P. C. K.; Hansen, O.; Stephens, I. E. L.; Kibsgaard, J.; Chorkendorff, I. Impact of nanoparticle size and lattice oxygen on water oxidation on NiFeOxHy. *Nat. Catal.* **2018**, *1*, 820–829.

(6) Díaz-Coello, S.; García, G.; Arévalo, M.; Pastor, E. Precise determination of Tafel slopes by DEMS. Hydrogen evolution on tungsten-based catalysts in alkaline solution. *Int. J. Hydrog. Energy* **2019**, *44*, 12576–12582.

(7) Wohlfahrt-Mehrens, M.; Heitbaum, J. Oxygen evolution on Ru and RuO2 electrodes studied using isotope labelling and on-line mass spectrometry. *J. Electroanal. Chem. Interf. Electrochem.* **1987**, *237*, 251–260.

(8) Winiwarter, A.; Silvioli, L.; Scott, S. B.; Enemark-Rasmussen, K.; Sariç, M.; Trimarco, D. B.; Vesborg, P. C. K.; Moses, P. G.; Stephens, I. E. L.; Seger, B.; Rossmeisl, J.; Chorkendorff, I. Towards an atomistic understanding of electrocatalytic partial hydrocarbon oxidation: propene on palladium. *Energy Environ. Sci.* **2019**, *12*, 1055–1067.

(9) Anastasijevic, N.; Baltruschat, H.; Heitbaum, J. DEMS as a tool for the investigation of dynamic processes: galvanostatic formic acid oxidation on a Pt electrode. *J. Electroanal. Chem. Interf. Electrochem.* **1989**, *272*, 89–100.

(10) Kasian, O.; Grote, J.-P.; Geiger, S.; Cherevko, S.; Mayrhofer, K. J. J. The Common Intermediates of Oxygen Evolution and Dissolution Reactions during Water Electrolysis on Iridium. *Angew. Chem. Int.* **2018**, *57*, 2488–2491.

(11) Bernhard, R.; Meini, S.; Gasteiger, H. A. On-Line Electrochemical Mass Spectrometry Investigations on the Gassing Behavior of Li 4 Ti 5 O 12 Electrodes and Its Origins. *J. Electrochem. Soc.* **2014**, *161*, A497–A505.

(12) Bernhard, R.; Metzger, M.; Gasteiger, H. A. Gas Evolution at Graphite Anodes Depending on Electrolyte Water Content and SEI Quality Studied by On-Line Electrochemical Mass Spectrometry. *J. Electrochem. Soc.* **2015**, *162*, A1984–A1989.

(13) Berkes, B. B.; Jozwiuk, A.; Vračar, M.; Sommer, H.; Brezesinski, T.; Janek, J. Online Continuous Flow Differential Electrochemical Mass Spectrometry with a Realistic Battery Setup for High-Precision, Long-Term Cycling Tests. *Anal. Chem.* **2015**, *87*, 5878–5883.

(14) Streich, D.; Guéguen, A.; Mendez, M.; Chesneau, F.; Novák, P.; Berg, E. J. Online Electrochemical Mass Spectrometry of High Energy Lithium Nickel Cobalt Manganese Oxide/Graphite Half- and Full-Cells with Ethylene Carbonate and Fluoroethylene Carbonate Based Electrolytes. *J. Electrochem. Soc.* **2016**, *163*, A964–A970.

(15) Khanipour, P.; Löffler, M.; Reichert, A. M.; Haase, F. T.; Mayrhofer, K. J. J.; Katsounaros, I. Electrochemical Real-Time Mass Spectrometry (EC-RTMS): Monitoring Electrochemical Reaction Products in Real Time. *Angew. Chem.* **2019**, *131*, 7351–7355.

(16) Trimarco, D. B.; Scott, S. B.; Thilsted, A. H.; Pan, J. Y.; Pedersen, T.; Hansen, O.; Chorkendorff, I.; Vesborg, P. C. Enabling real-time detection of electrochemical desorption phenomena with sub-monolayer sensitivity. *Electrochim. Acta* **2018**, *268*, 520–530.

(17) Scott, S. B.; Engstfeld, A. K.; Jusys, Z.; Hochfilzer, D.; Knøsgaard, N.; Trimarco, D. B.; Vesborg, P. C. K.; Behm, R. J.; Chorkendorff, I. Anodic molecular hydrogen formation on Ru and Cu electrodes. *Catal. Sci. Technol.* **2020**, *10*, 6870–6878.

(18) Lewis, N. S.; Nocera, D. G. Powering the planet: Chemical challenges in solar energy utilization. *Proc. Natl. Acad. Sci. U. S. A.* **2006**, *103*, 15729–15735.

(19) Clark, E. L.; Singh, M. R.; Kwon, Y.; Bell, A. T. Differential Electrochemical Mass Spectrometer Cell Design for Online Quantification of Products Produced during Electrochemical Reduction of CO 2. *Anal. Chem.* **2015**, *87*, 8013–8020.

(20) Wonders, A.; Housmans, T.; Rosca, V.; Koper, M. On-line mass spectrometry system for measurements at single-crystal electrodes in hanging meniscus configuration. *J. Appl. Electrochem* **2006**, *36*, 1215–1221.

(21) Harris, C. R. et al. Array programming with NumPy. *Nature* **2020**, *585*, 357–362.

(22) Scott, S. B.; Kibsgaard, J.; Vesborg, P. C.; Chorkendorff, I. Tracking oxygen atoms in electrochemical CO oxidation – Part I: Oxygen exchange via CO2 hydration. *Electrochim. Acta* **2021**, *374*, 137842.

(23) Henriksen, T. R.; Olsen, J. L.; Vesborg, P.; Chorkendorff, I.; Hansen, O. Highly sensitive silicon microreactor for catalyst testing. *Rev. Sci. Instrum.* **2009**, *80*, 124101.

(24) Trimarco, D. B. Real-time detection of sub-monolayer desorption phenomena during electrochemical reactions: Instrument development and applications. Ph.D. thesis, Danish Technical University, 2017.

(25) Scott, S. B. Isotope-Labeling Studies in Electrocatalysis for Renewable Energy Conversion. Ph.D. thesis, Danish Technical University, 2019.

(26) Hansen, P. C. Deconvolution and Regularization with Toeplitz Matrices. *Numer. Algorithms* **2002**, *29*, 323–378.

(27) Levenspiel, O.; Bischoff, K. B. In *Patterns of Flow in Chemical Process Vessels*; Drew, T. B., Hoopes, J. W., Vermeulen, T., Eds.; Advances in Chemical Engineering; Academic Press, 1964; Vol. 4; pp 95 – 198.

(28) Cussler, E. L. *Diffusion: Mass Transfer in Fluid Systems*, 2nd ed.; Cambridge University Press: New York, 1997.

(29) Ferrell, R. T.; Himmelblau, D. M. Diffusion coefficients of hydrogen and helium in water. *AIChE J .* **1967**, *13*, 702–708.

(30) Sander, R. Compilation of Henry's law constants (version 4.0) for water as solvent. *Atmos. chem. phys.* **2015**, *15*, 4399–4981.

(31) Conway, B.; Bai, L. Determination of adsorption of OPD H species in the cathodic hydrogen evolution reaction at Pt in relation to electrocatalysis. *J. Electroanal. Chem. Interf. Electrochem.* **1986**, *198*, 149–175.

(32) Marković, N. M.; Grgur, B. N.; Ross, P. N. Temperature-Dependent Hydrogen Electrochemistry on Platinum Low-Index Single-Crystal Surfaces in Acid Solutions. *J. Phys. Chem. B* **1997**, *101*, 5405–5413.

(33) Bard, A. J.; Faulkner, L. R. *Electrochemical Methods: Fundamentals and Applications*, 2nd ed.; Wiley: New York, 2000; p 864.

(34) Schultze, J.; Vetter, K. The influence of the tunnel probability on the anodic oxygen evolution and other redox reactions at oxide covered platinum electrodes. *Electrochim. Acta* **1973**, *18*, 889–896.

(35) Vetter, K.; Schultze, J. The kinetics of the electrochemical formation and reduction of monomolecular oxide layers on platinum in 0.5 M H2SO4. *J. Electroanal. Chem. Interf. Electrochem.* **1972**, *34*, 131–139.

(36) Jain, A.; Ong, S. P.; Hautier, G.; Chen, W.; Richards, W. D.; Dacek, S.; Cholia, S.; Gunter, D.; Skinner, D.; Ceder, G.; Persson, K. a. Commentary: The Materials Project: A materials genome approach to accelerating materials innovation. *APL Mater.* **2013**, *1*, 011002.

(37) Rossmeisl, J.; Logadottir, A.; Nørskov, J. Electrolysis of water on (oxidized) metal surfaces. *Chem. Phys.* **2005**, *319*, 178–184.

(38) Kim, C.; Weng, L.-C.; Bell, A. T. Impact of Pulsed Electrochemical Reduction of CO 2 on the Formation of C 2+ Products over Cu. *ACS catal.* **2020**, 12403–12413.

(39) Andersen, S. Z.; Statt, M. J.; Bukas, V. J.; Shapel, S. G.; Pedersen, J. B.; Krempl, K.; Saccoccio, M.; Chakraborty, D.; Kibsgaard, J.; Vesborg, P. C. K.; Nørskov, J.; Chorkendorff, I. Increasing stability, efficiency, and fundamental understanding of lithium-mediated electrochemical nitrogen reduction. *Energy Environ. Sci.* **2020**, *13*, 4291–4300.

(40) Kimura, K. W.; Fritz, K. E.; Kim, J.; Suntivich, J.; Abruña, H. D.; Hanrath, T. Controlled Selectivity of CO 2 Reduction on Copper by Pulsing the Electrochemical Potential. *ChemSusChem* **2018**, *11*, 1781–1786.

(41) Gopeesingh, J.; Ardagh, M. A.; Shetty, M.; Burke, S. T.; Dauenhauer, P. J.; Abdelrahman, O. A. Resonance-Promoted Formic Acid Oxidation via Dynamic Electrocatalytic Modulation. *ACS catal.* **2020**, *10*, 9932–9942.

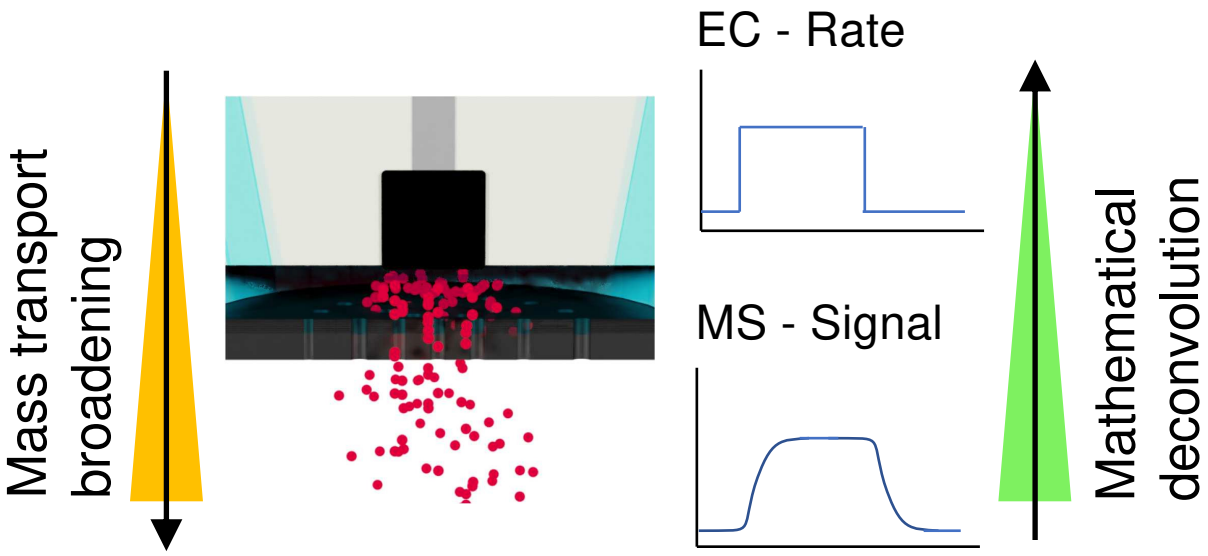


Figure 6: For Table of Contents Only.